

Quasiparticle Scattering Interference in Superconducting Iron-pnictides

Yan-Yang Zhang,¹ Chen Fang,¹ Xiaoting Zhou,¹ Kangjun Seo,¹
Wei-Feng Tsai,¹ B. Andrei Bernevig,² and Jiangping Hu¹

¹*Department of Physics, Purdue University, West Lafayette, Indiana 47907, USA*

²*Princeton Center for Theoretical Science, Princeton University, NJ 08544*

(Dated: October 30, 2018)

Using both two orbital and five orbital models, we investigate the quasiparticle interference (QPI) patterns in the superconducting (SC) state of iron-based superconductors. We compare the results for nonmagnetic and magnetic impurities in sign-changed s-wave $\cos(k_x) \cdot \cos(k_y)$ and sign-unchanged $|\cos(k_x) \cdot \cos(k_y)|$ SC states. While the patterns strongly depend on the chosen band structure details, the sensitivity of peaks around $(\pm\pi, 0)$ and $(0, \pm\pi)$ wavevectors on magnetic or non-magnetic impurities, and on sign-changed or sign-unchanged SC orders is a common feature. Our results strongly suggest that the QPI can provide a direct evidence of the pairing symmetry in the SC states.

PACS numbers: 74.25Jb, 74.20-z

I. INTRODUCTION

Recently, the discovery of high temperature superconductivity in oxypnictide compounds^{1,2,3,4,5} stirred great interests in the condensed matter community. One important problem is to elucidate the pairing symmetry of the order parameter of the superconducting state. Theoretically many possible gap pairing symmetries have been proposed. Due to the proximity of the superconducting state to a collinear antiferromagnetic state, a magnetism-based mechanism has emerged in both the weak and strong coupling approaches. This mechanism suggests that an extended s-wave pairing symmetry is favored^{6,7,8}.

The weak-coupling approach favors an s-wave (so called s_{\pm}) state⁷ in which the relative sign of order parameters changes between the hole and electron pockets. However, the weak-coupling approach does not specify the exact form of order parameter. In a recent paper⁶, we showed that, in strong-coupling, the pairing symmetry is determined mainly by the next nearest neighbor antiferromagnetic exchange coupling J_2 ^{9,10,11} and has an explicit $s_{x^2-y^2}$ form in momentum space, $\cos(k_x) \cdot \cos(k_y)$. This result is completely independent of any model, *as long as* the dominating interaction is next-nearest neighbor J_2 and the Fermi surfaces are located close to the Γ and M points in the Brillouin zone. The $\cos(k_x) \cdot \cos(k_y)$ changes sign between the electron and hole pockets in the Brillouin zone. In this sense, it resembles the order parameter, s_{\pm} , proposed through general weak-coupling arguments⁷.

The magnitudes of superconducting gaps measured by angle-resolved photo-emission spectroscopy (ARPES) on different Fermi surfaces are in good agreement with the simple $\cos(k_x) \cdot \cos(k_y)$ ^{12,13,14}. The magnetic properties in the SC state have also been shown to be consistent with the proposed pairing symmetry^{15,16,17,18}. Although several theoretical works^{19,20,21,22} propose different ways to measure the sign change between the electron and hole pockets, directly probing this change is still a fundamental experimental challenge. Without any detailed cal-

culations, a theoretical suggestion for probing the sign change through quasiparticle interference (QPI) in the presence of magnetic and nonmagnetic impurities, has been made in⁸.

The QPI can be probed directly in modern STM experiments^{23,24} and has been intensively studied in copper-based high temperature superconductors. In the presence of impurities, elastic scattering mixes two eigenstates with different momentum \mathbf{k}_1 and \mathbf{k}_2 on the same contour of constant energy and a scattering interference pattern appears as a modulation in the local density states (LDOS) at wavevector $\mathbf{q} = \mathbf{k}_2 - \mathbf{k}_1$. Such kind of interference pattern in the wavevector space can be observed in the Fourier transform scanning tunneling spectroscopy (FT-STs)^{25,26}. The quasiparticle scattering between regions in the \mathbf{k} space with high density of states (DOS) yields peaks or arcs in the FT-STs. For example, in the d-wave pairing SC state, many QPI dispersive peaks can be identified; in the cuprates, they provide details of the band structure, the nature of superconducting gap, or other competing orders^{27,28,29,30,31,32,33,34,35,36,37,38,39}.

In this paper, we perform a detailed investigation of the QPI in iron-based superconductors. We use both two orbital and five orbital models. In general, the QPI strongly depends on the bare band structure. The QPI patterns change significantly from a two orbital model to a five-orbital one, which suggests that the QPI can provide direct information of the detailed band structure and orbital degrees of freedom. By carefully examining the pattern, we can also identify common features of the QPI pattern in both models, which are tied to the symmetry of SC order parameter and the impurity type. These general features include: (1) The intra-orbital scattering by impurities always dominates the inter-orbital scattering. The latter has negligible effect on the QPI (though it breaks discrete C_4 symmetry of the patterns); (2) Unlike in the d-wave SC state of cuprates where a large density of states at the banana tips cause dispersive features in the QPI²⁵, the nodeless s-wave has lit-

the density of states inside SC gaps and hence no strong points dominate the scattering; (3) A magnetic impurity always causes a broad and large peak near $\mathbf{q} = (0, 0)$ in the QPI; this stems from intra-band scattering. For a non-magnetic impurity, the intensity around $\mathbf{q} = (0, 0)$ is small. This result can be used to distinguish two types of impurities; (4) The peaks around $(\pm\pi, 0)$ and $(0, \pm\pi)$ are sensitive to both the type of impurities and to the sign change of the SC orders between the electron and hole pockets. Magnetic impurities along with sign-unchanged SC orders or non-magnetic impurity with sign-changed SC orders cause strong interference peaks. Finally, as in a fully-gapped s-wave SC state the results from a full T-matrix calculation do not differ considerably from results of a simple first order perturbation calculation^{40,41}, we are able to also provide an analytic derivation of the above results.

II. TWO-ORBITAL MODEL AND SINGLE IMPURITY SCATTERING

We first investigate the QPI in a simple two orbital model^{6,15,42}. The mean field Hamiltonian of the model in SC states is written as $H = \sum_{\mathbf{k}} \Psi^\dagger(\mathbf{k})B(\mathbf{k})\Psi(\mathbf{k})$ with

$$B(\mathbf{k}) = \begin{pmatrix} \epsilon_x(\mathbf{k}) - \mu & \Delta_1(\mathbf{k}) & \epsilon_{xy}(\mathbf{k}) & 0 \\ \Delta_1^*(\mathbf{k}) & -\epsilon_x(\mathbf{k}) + \mu & 0 & -\epsilon_{xy}(\mathbf{k}) \\ \epsilon_{xy}(\mathbf{k}) & 0 & \epsilon_y(\mathbf{k}) - \mu & \Delta_2(\mathbf{k}) \\ 0 & -\epsilon_{xy}(\mathbf{k}) & \Delta_2^*(\mathbf{k}) & -\epsilon_y(\mathbf{k}) + \mu \end{pmatrix}, \quad (1)$$

where $\Psi^\dagger(\mathbf{k}) = (c_{1,\mathbf{k},\uparrow}^\dagger, c_{1,-\mathbf{k},\downarrow}, c_{2,\mathbf{k},\uparrow}^\dagger, c_{2,-\mathbf{k},\downarrow})$ in the Nambu formalism. The single-particle bands read

$$\begin{aligned} \epsilon_x(k_x, k_y) &= -2t_1 \cos k_x - 2t_2 \cos k_y - 4t_3 \cos k_x \cos k_y \\ \epsilon_y(k_x, k_y) &= \epsilon_x(k_y, k_x), \quad \epsilon_{xy}(k_x, k_y) = -4t_4 \sin k_x \sin k_y, \end{aligned}$$

where $t_1 = -1$, $t_2 = 1.3$, $t_3 = t_4 = -0.85$ and μ is chosen in the electron-doped regime. Hereafter, $|t_1|$ will be used as the energy unit. For $s_{x^2y^2}$ -wave pairing, the order parameter is $\Delta_1(k_x, k_y) = \Delta_2(k_x, k_y) = \Delta_0 \cos k_x \cos k_y$ ^{6,15}.

The Green's function for the clean system is

$$G^0(\mathbf{k}, \omega) \equiv G^0(\mathbf{k}, \mathbf{k}, \omega) = [(\omega + i\delta)I - B(\mathbf{k})]^{-1}, \quad (2)$$

where I is the identity matrix and δ is the energy width broadening. In this work, we only consider a single impurity with potential $\sim \delta(\mathbf{x})$ so that the impurity matrix $V(\mathbf{k}_1, \mathbf{k}_2) = V$ is independent of \mathbf{k} . The impurity induced Green's function is expressed as

$$\delta G(\mathbf{k}_1, \mathbf{k}_2, \omega) = G^0(\mathbf{k}_1, \omega)T(\mathbf{k}_1, \mathbf{k}_2, \omega)G^0(\mathbf{k}_2, \omega). \quad (3)$$

Standard perturbation theory gives

$$\begin{aligned} T(\omega) &= V + VT^0(\omega)V + VT^0(\omega)VT^0(\omega)V + \dots \\ &= [I - VT^0(\omega)]^{-1}V, \end{aligned} \quad (4)$$

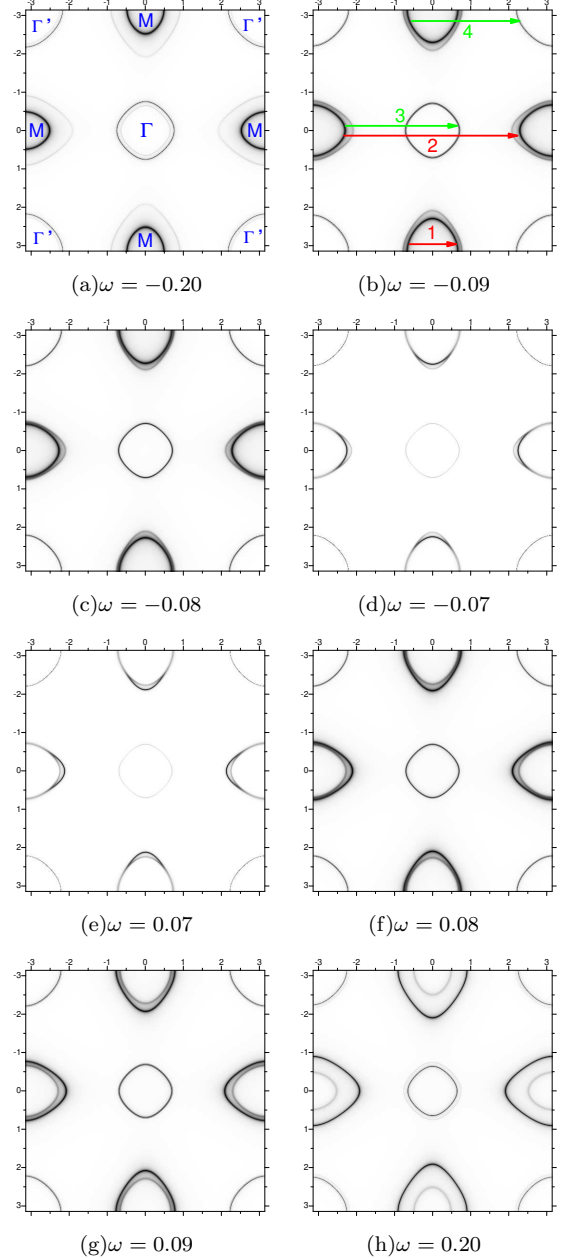


FIG. 1: The spectral function $\mathcal{A}(\mathbf{k}, \omega)$ in the unfolded Brillouin zone, for $s_{x^2y^2}$ with $\Delta_0 = 0.1$. Darker regions correspond to larger values of \mathcal{A} hence larger DOS in \mathbf{k} space.

where

$$\Gamma^0(\omega) = \int \frac{d^2k}{(2\pi)^2} G^0(\mathbf{k}, \omega). \quad (5)$$

Consequently, the Fourier transform of the (induced) local density of states is

$$\delta\rho(\mathbf{q}, \omega) = \frac{i}{2\pi} \int \frac{d^2k}{(2\pi)^2} g(\mathbf{k}, \mathbf{q}, \omega), \quad (6)$$

where $\mathbf{q} = \mathbf{k}' - \mathbf{k}$ and

$$g(\mathbf{k}, \mathbf{q}, \omega) = \delta G_{11}(\mathbf{k}, \mathbf{k}', \omega) - \delta G_{11}^*(\mathbf{k}', \mathbf{k}, \omega) + \delta G_{33}(\mathbf{k}, \mathbf{k}', \omega) - \delta G_{33}^*(\mathbf{k}', \mathbf{k}, \omega). \quad (7)$$

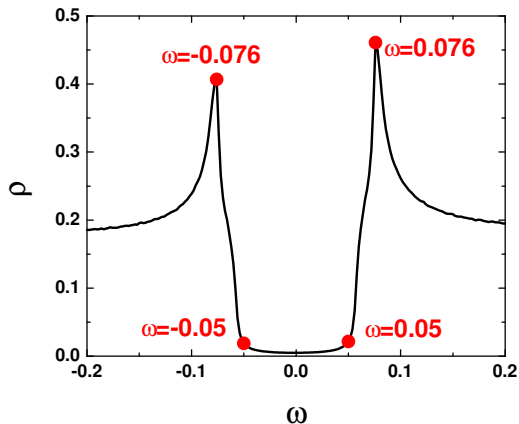


FIG. 2: Bulk density of states ρ for $s_{x^2-y^2}$ as a function of ω , $\Delta_0 = 0.1$ and no impurities. Some special values are marked by red dots. The energy broadening width is $\delta = 0.002$.

Due to the multi-orbital nature of the band model, we distinguish different types of impurities. They are

$$V = V_{\text{intra}} = I \otimes \begin{pmatrix} V_0 & 0 \\ 0 & \pm V_0 \end{pmatrix}, \quad (8)$$

for an impurity with only intra-orbital scattering, and

$$V = V_{\text{inter}} = \sigma_x \otimes \begin{pmatrix} V_0 & 0 \\ 0 & \pm V_0 \end{pmatrix}, \quad (9)$$

for inter-orbital scattering, where the upper (down) sign corresponds to magnetic (non-magnetic) impurity. Since it was argued that for cuprate superconductors this T -matrix method is valid when impurity scattering strength is much larger than the maximal pairing gap²⁴, we take $V_0 = 4\Delta_0$ in our calculation. Our following results do not depend on V_0 as long as V_0 is much larger than Δ_0 .

A. Numerical results

We first calculate electronic properties in an impurity-free system. Most of the results in this section have been already computed in less detail in¹⁵. In Fig. 1, we plot the spectral function

$$\mathcal{A}(\mathbf{k}, \omega) = -\frac{1}{\pi} \text{Im}[G_{11}^0(\mathbf{k}, \omega) + G_{33}^0(\mathbf{k}, \omega)] \quad (10)$$

of the clean system at different ω . The typical value of order parameter $\Delta_0 = 0.1$ will be used throughout this paper. It should be noted that for ω and $-\omega$, the shapes (topology) of the contours of constant energy (CCE) are

almost identical, but the numerical values of \mathcal{A} on these contours are remarkably different. As an example, let us focus on the regions near one of the M points $(\pi, 0)$, where the CCE consists of two semi-oval-circles, or two complete oval-circles due to the periodicity of the Brillouin zone (BZ). As can be seen from Fig. 1 (a) and (b), for negative ω , the spectral weight on the inner circle is larger than that on the outer one. The situation is opposite for positive ω (Fig. 1 (g) and (h)). This leads to different scattering interference patterns at $\pm\omega$, as we will see later on.

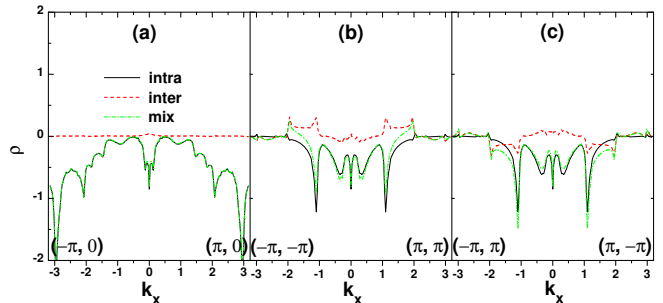


FIG. 3: (color online) $\delta\rho(\mathbf{q}, \omega = 0.07)$ for non-magnetic impurity with V_{intra} (black solid), V_{inter} (red dash) and $V_{\text{mix}} \equiv V_{\text{intra}} + V_{\text{inter}}$ (green dash dot) along three directions: (a) $(-\pi, 0) \rightarrow (\pi, 0)$, (b) $(-\pi, -\pi) \rightarrow (\pi, \pi)$ and (c) $(-\pi, \pi) \rightarrow (\pi, -\pi)$.

The bulk density of states $\rho(\omega) = \sum_{\mathbf{k}} \mathcal{A}(\mathbf{k}, \omega)$ is plotted in Fig. 2. It is fully gaped within $\sim (-0.05, 0.05)$ and the coherent peak occurs at $\sim \pm 0.076$ ¹⁵.

To exemplify some scattering amplitudes, we plot $\delta\rho(\mathbf{q})$ for a non-magnetic impurity near the edge of the gap ($\omega = 0.07$) along three special directions in Fig. 3. Two observations in these figures are common to all our results. First, $\rho(\mathbf{q})$ for inter-orbital scattering in the two diagonal directions are quite different (compare the red dash lines in Fig. 3 (b) and (c)). This is not surprising since the inter-orbital scattering such as $c_{1,\mathbf{k},\uparrow}^\dagger c_{2,\mathbf{k},\uparrow}$ breaks the symmetry between directions $(-\pi, -\pi) \rightarrow (\pi, \pi)$ and $(-\pi, \pi) \rightarrow (\pi, -\pi)$. Second, the amplitude of intra-orbital impurity is stronger than that of the inter-orbital one; therefore the intra-orbital scattering is dominant when both are present. As such, in the following, we present only numerical results for intra-orbital impurities.

In Fig. 4 and Fig. 5, we show the two-dimensional contour of the scattering pattern $\delta\rho(\mathbf{q})$ for non-magnetic and magnetic impurities, respectively. The $\delta\rho(\mathbf{q})$ profiles along special directions are plotted in Fig 6. In Figs. 4 and 5, the most prominent features for all ω values are two intersecting ovals (see also the peaks directed by red arrows in Fig. 6), reflecting the strong intra-pocket scattering between equal-energy curves near M points with the largest DOS. These scattering processes are labeled by red arrows (1 and 2) in Fig. 1 (b), where scattering wavevectors outside the first BZ (e.g., arrow 2) should be

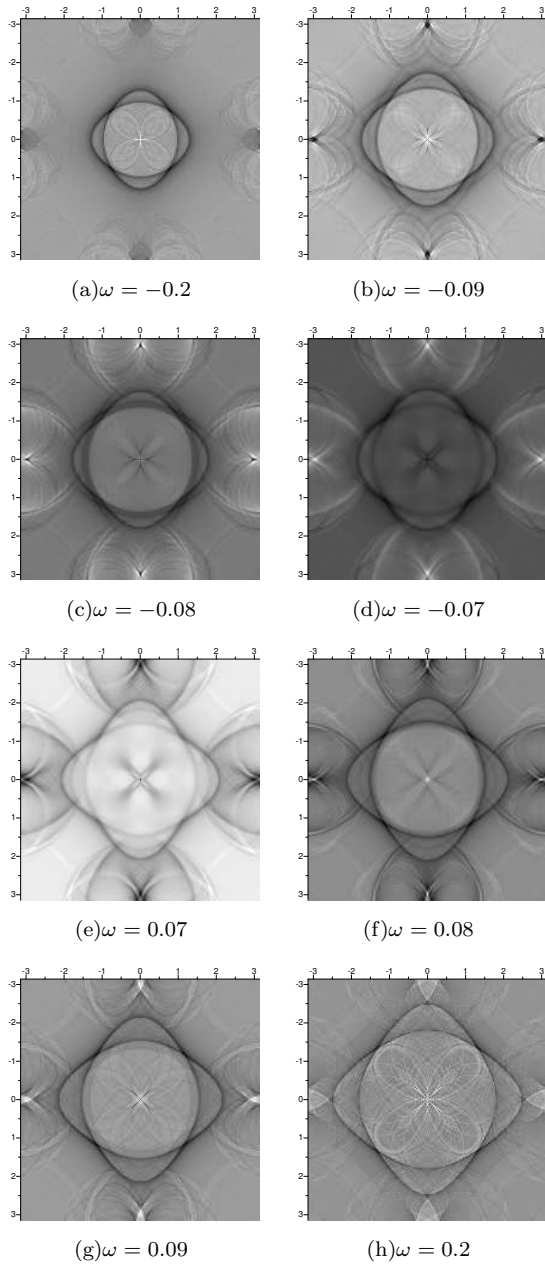


FIG. 4: $\delta\rho(\mathbf{q})$ for non-magnetic impurity with intra-orbital scattering, $V_0 = 0.4$. A 200×200 lattice in \mathbf{k} -space is used in numerical integration of equation (5) and the energy broadening width $\delta = 0.005$.

understood as their equivalent counterparts in the first BZ. By increasing $|\omega|$ on the negative (positive) energy side, the size of the ovals decreases (increases) because the important scattering takes place between the inner (outer) circle of CCE near M with the largest DOS. At a definite energy ω , this gives two peaks along direction $M \rightarrow \Gamma$, corresponding to the scattering along the major and minor axis of the oval CCE respectively. Due to the congruence of these CCE oval circles, they always intersect on the diagonal line ($\Gamma' \rightarrow \Gamma$), therefore only one peak can be observed along this direction. For ω far out-

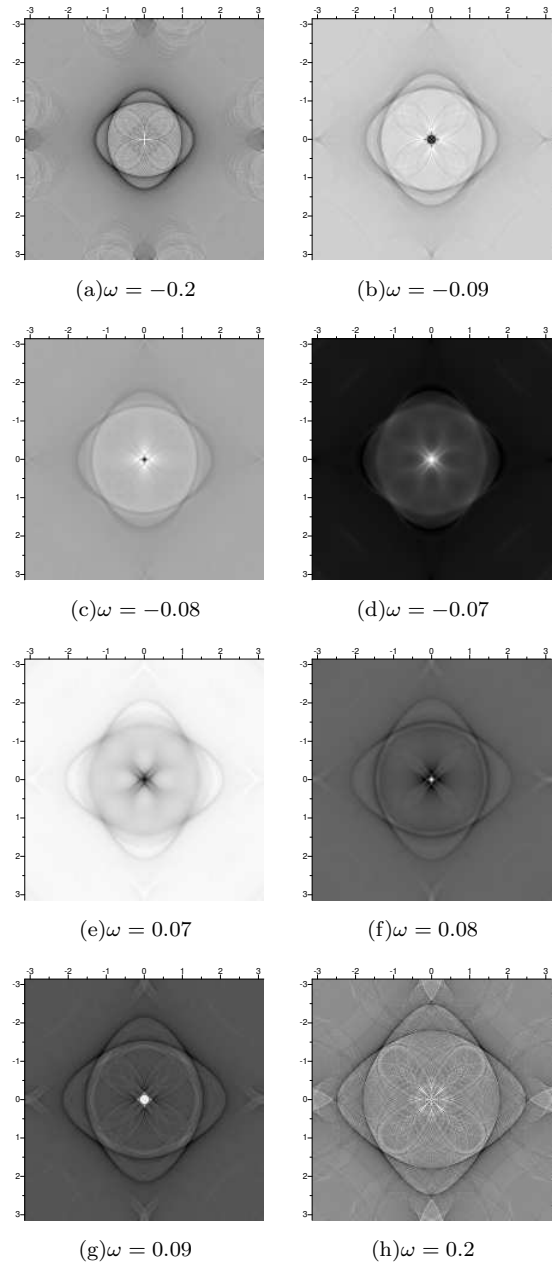


FIG. 5: The same with Fig. 4 but for magnetic impurity, $V_0 = 0.4$.

side the gap, there is no noticeable difference between the magnetic and non-magnetic impurities (compare Fig. 4 (a) and (h) with Fig. 5 (a) and (h)). This is understandable since the tendency of the (Cooper) pair breaking due to a magnetic impurity is most significant near the Fermi level. Within the single-particle scattering regime considered here, for $|\omega| < 0.05$ inside the gap, no interference pattern is expected due to lack of scattering states. This is confirmed (but not shown here) by the fact that, when decreasing the imaginary part of the energy δ in Green's functions, the peaks of $\delta\rho(\mathbf{q}, |\omega| > 0.05)$ are sharper, while $\delta\rho(\mathbf{q}, |\omega| < 0.05)$ vanish trivially for all \mathbf{q} .

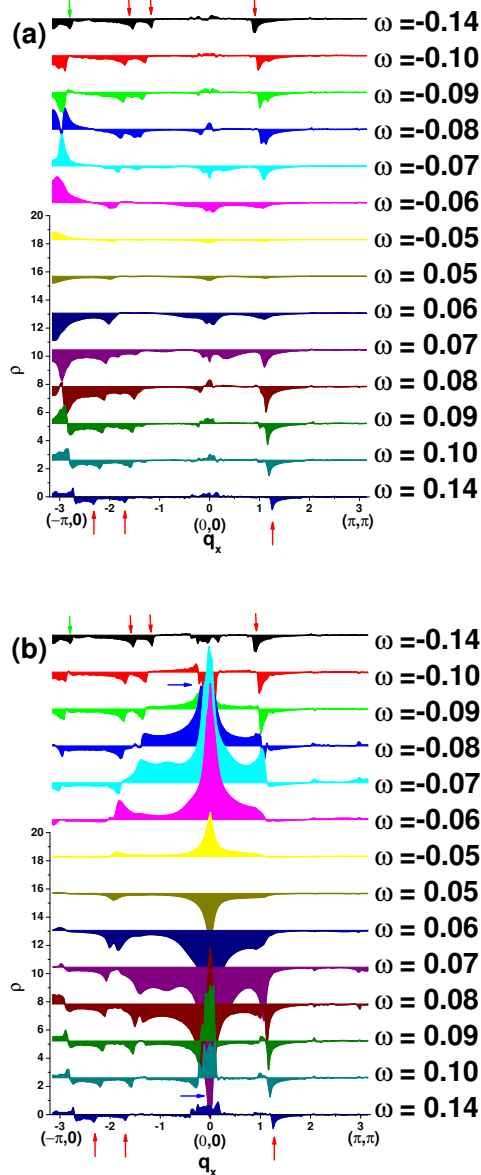


FIG. 6: (color online) Profiles of $\delta\rho(\mathbf{q}, \omega)$ along $M \rightarrow \Gamma \rightarrow \Gamma'$ for (a) non-magnetic impurity and (b) magnetic impurity. The data are shifted vertically relative to each other for clarity.

There are additional peaks around the M points, as directed by green arrows in Fig. 6, which play an important role in distinguishing different types of impurities. When decreasing $|\omega|$, they move steadily toward M. These originate from the inter-pocket scattering as demonstrated by green arrows (3 and 4) in Fig. 1 (b). The differences of these peaks between non-magnetic and magnetic impurities are clear near the gap edges, suggesting strong dependence on coherent factors due to impurities, as well as on DOS contour of the clean system^{24,40}. For non-magnetic impurity (Fig. 6 (a)), the peaks are much more sharper.

Moreover, a large peak appears around Γ (blue arrows in (Fig. 6 (b)). This suggests that the magnetic impurity's ability to localize the quasiparticle is weaker than that of the non-magnetic one.

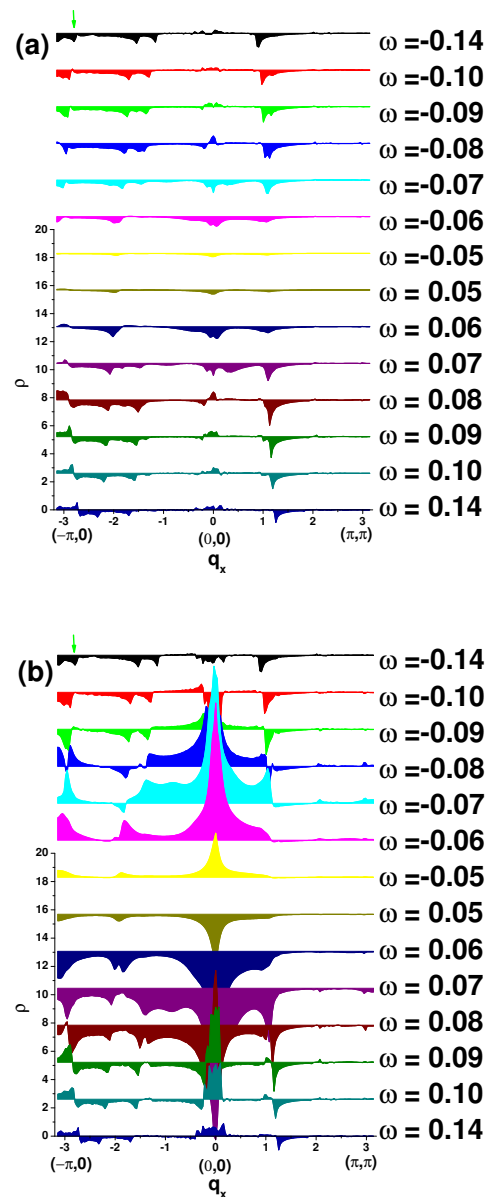


FIG. 7: (color online) Same as Fig. 6 but for the case without sign change, $\Delta_1(k_x, k_y) = \Delta_2(k_x, k_y) = |\Delta_0 \cos k_x \cos k_y|$. (a) Non-magnetic impurity and (b) magnetic impurity.

B. The effect of sign change

The $s_{x^2y^2}$ pairing differs from the conventional s -wave pairing that it changes sign in the BZ. To investigate the physical consequence of this effect, we artificially prohibit this sign change by letting $\Delta_1(k_x, k_y) = \Delta_2(k_x, k_y) =$

$|\Delta_0 \cos k_x \cos k_y|$ in Eq. (1). This may not correspond to any realistic physical system, but can reveal, by comparison, the effects of the sign change of the order parameter. We show the profile of $\delta\rho(\mathbf{q})$ in Fig. 7. The most observable feature is that, contrary to the sign-change case, the inter-pocket peak around the M point is now sharper for the magnetic impurity.

C. The QPI in other pairing symmetry

We briefly discuss the $d_{x^2-y^2}$ pairing symmetry as an example of a case with gapless nodal quasiparticles. The energy contours and interference patterns are plotted in Fig. 8, Fig. 9 and Fig. 10. Besides the robust intra-pocket scattering around Γ and the impurity-type sensitive peaks near $(\pm\pi, 0)$ and $(0, \pm\pi)$, the most specific feature is the finite DOS within the pseudo-gap $\omega \in (-0.05, 0.05)$, giving rise to small but finite QPI in this region, as can be seen in (e), (f) and (g) of Figs. 9 and 10. This originates from the intra-hole pocket scattering. When $|\omega| \rightarrow 0$, the QPI concentrates on the diagonal directions as expected from the band structures in Fig 8.

D. Analytical analysis

We now try to understand the above numerical results analytically. The two-orbital Hamiltonian can be diagonalized by a unitary transformation

$$U^\dagger(\mathbf{k}) \begin{pmatrix} \epsilon_x(\mathbf{k}) & \epsilon_{xy}(\mathbf{k}) \\ \epsilon_{xy}(\mathbf{k}) & \epsilon_y(\mathbf{k}) \end{pmatrix} U(\mathbf{k}) = \begin{pmatrix} \epsilon_1(\mathbf{k}) & 0 \\ 0 & \epsilon_2(\mathbf{k}) \end{pmatrix}, \quad (11)$$

where

$$U = \begin{pmatrix} \cos(\theta_{\mathbf{k}}/2) & -\sin(\theta_{\mathbf{k}}/2) \\ \sin(\theta_{\mathbf{k}}/2) & \cos(\theta_{\mathbf{k}}/2) \end{pmatrix}, \quad (12)$$

and $\tan(\theta_{\mathbf{k}}) = \frac{2\epsilon_{xy}(\mathbf{k})}{\epsilon_x(\mathbf{k}) - \epsilon_y(\mathbf{k})}$. The integral over BZ in calculating the T -matrix in Eq. (5) makes the analytical treatment untractable. Fortunately we numerically verified that for the strength of impurity in this work ($V_0 = 0.4$), the first order expansion in Eq. (4) is sufficiently precise (with error less than 2%). In the following, we safely take $T = V$. In the band-basis, the V -matrix for intra-orbital impurity is in the following \mathbf{k} -dependent form

$$V(\mathbf{k}, \mathbf{k}') = \begin{pmatrix} \cos(\frac{\theta_{\mathbf{k}} - \theta_{\mathbf{k}'}}{2}) & \sin(\frac{\theta_{\mathbf{k}} - \theta_{\mathbf{k}'}}{2}) \\ -\sin(\frac{\theta_{\mathbf{k}} - \theta_{\mathbf{k}'}}{2}) & \cos(\frac{\theta_{\mathbf{k}} - \theta_{\mathbf{k}'}}{2}) \end{pmatrix} \otimes \begin{pmatrix} V_0 & 0 \\ 0 & \pm V_0 \end{pmatrix}, \quad (13)$$

where the upper (lower) sign is for the magnetic (non-magnetic) impurity, as in Eqs. (8) and (9). The induced Green's function in Eq. (3) can now be transformed to the band representation. After a lengthy but straightforward calculation, we obtain

$$\begin{aligned} \delta\rho(\mathbf{q}) = & [P_1(\mathbf{k}, \mathbf{q}) + P_2(\mathbf{k}, \mathbf{q})] V_0 \cos^2\left(\frac{\theta_{\mathbf{k}} - \theta_{\mathbf{k}+\mathbf{q}}}{2}\right) \\ & + [Q_1(\mathbf{k}, \mathbf{q}) + Q_2(\mathbf{k}, \mathbf{q})] V_0 \sin^2\left(\frac{\theta_{\mathbf{k}} - \theta_{\mathbf{k}+\mathbf{q}}}{2}\right), \quad (14) \end{aligned}$$

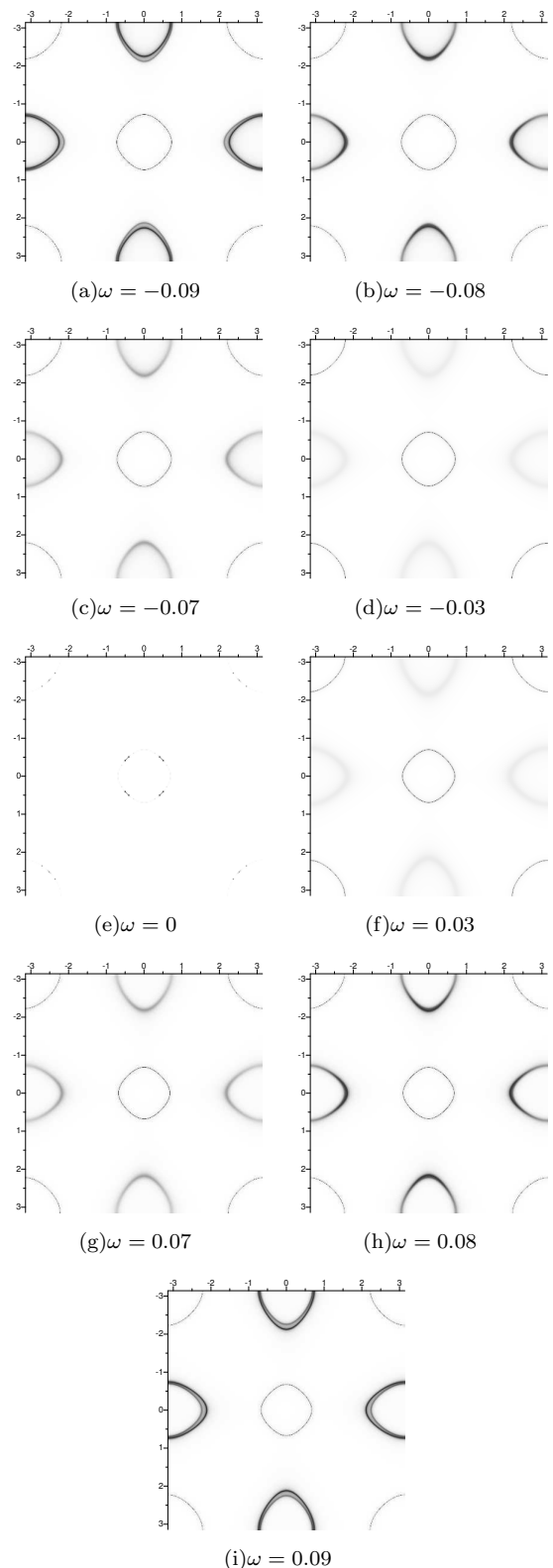


FIG. 8: The spectral function $\mathcal{A}(\mathbf{k}, \omega)$ for $d_{x^2-y^2}$ pairing symmetry with $\Delta_0 = 0.1$.

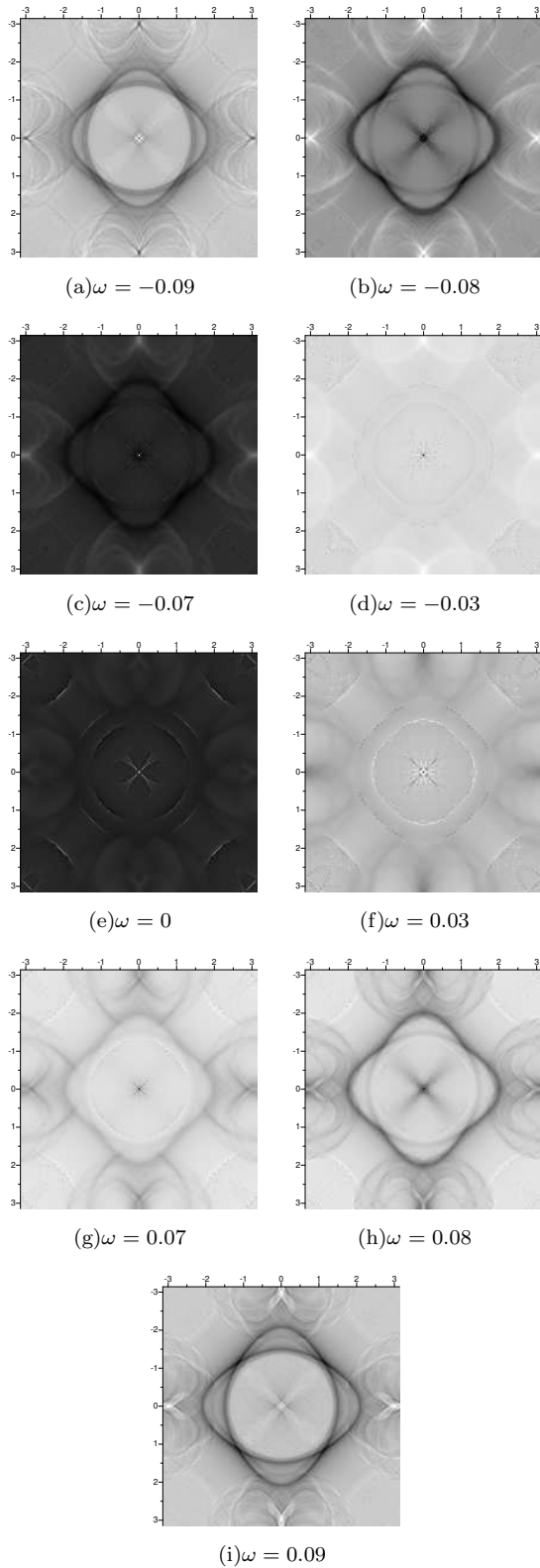


FIG. 9: $\delta\rho(\mathbf{q})$ for non-magnetic impurity for $d_{x^2-y^2}$ pairing symmetry with intra-orbital scattering, $V_0 = 0.4$.

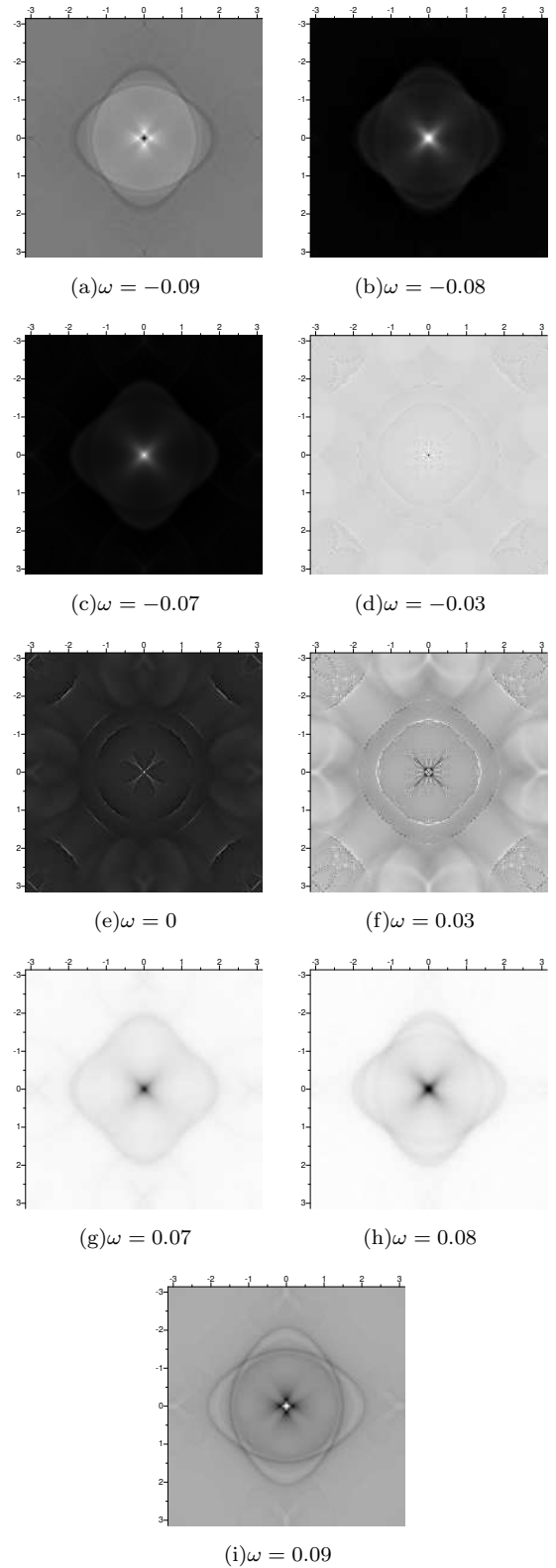


FIG. 10: The same with Fig. 9, but for magnetic impurity.

where P_i and Q_i denote the contributions from *intra-pocket* and *inter-pocket* scattering respectively, and take

$$\begin{aligned} P_{1(2)}(\mathbf{k}, \mathbf{q}) &= \frac{(\omega + \epsilon_{1(2)}(\mathbf{k}))(\omega + \epsilon_{1(2)}(\mathbf{k} + \mathbf{q})) \pm \Delta(\mathbf{k})\Delta(\mathbf{k} + \mathbf{q})}{(\omega^2 - \Delta(\mathbf{k})^2 - \epsilon_{1(2)}(\mathbf{k})^2)(\omega^2 - \Delta(\mathbf{k} + \mathbf{q})^2 - \epsilon_{1(2)}(\mathbf{k} + \mathbf{q})^2)}, \\ Q_{1(2)}(\mathbf{k}, \mathbf{q}) &= \frac{(\omega + \epsilon_{1(2)}(\mathbf{k}))(\omega + \epsilon_{2(1)}(\mathbf{k} + \mathbf{q})) \pm \Delta(\mathbf{k})\Delta(\mathbf{k} + \mathbf{q})}{(\omega^2 - \Delta(\mathbf{k})^2 - \epsilon_{1(2)}(\mathbf{k})^2)(\omega^2 - \Delta(\mathbf{k} + \mathbf{q})^2 - \epsilon_{2(1)}(\mathbf{k} + \mathbf{q})^2)}. \end{aligned} \quad (15)$$

From these expressions we see that, for $\omega \sim \pm\Delta(k_f)$, and on the energy contour $\epsilon_i(k) \sim 0$, the magnetic impurity contribution is almost zero if $q \sim (\pi, 0)$ for the sign-changing s-wave. The counterpart is true if Δ does not change sign: the contribution by magnetic impurity is now much larger than that by non-magnetic impurity. Furthermore, at $q \sim 0$ the contribution by magnetic impurity is much larger than the non-magnetic impurity. These are consistent with our numerical results and previous theoretical argument⁸.

Now let us turn to the inter-orbital case. After the same process, one obtains

$$V(\mathbf{k}, \mathbf{k}') = \begin{pmatrix} \cos(\frac{\theta_{\mathbf{k}+\theta_{\mathbf{k}'}}}{2}) & \sin(\frac{\theta_{\mathbf{k}+\theta_{\mathbf{k}'}}}{2}) \\ -\sin(\frac{\theta_{\mathbf{k}+\theta_{\mathbf{k}'}}}{2}) & \cos(\frac{\theta_{\mathbf{k}+\theta_{\mathbf{k}'}}}{2}) \end{pmatrix} \otimes \begin{pmatrix} V_0 & 0 \\ 0 & \pm V_0 \end{pmatrix} \quad (16)$$

The result is

$$\begin{aligned} \delta\rho(\mathbf{q}) &= [P_1(\mathbf{k}, \mathbf{q}) + P_2(\mathbf{k}, \mathbf{q})] V_0 \frac{\cos(\theta_{\mathbf{k}}) + \cos(\theta_{\mathbf{k}+\mathbf{q}})}{2} \\ &+ [Q_1(\mathbf{k}, \mathbf{q}) + Q_2(\mathbf{k}, \mathbf{q})] V_0 \frac{\cos(\theta_{\mathbf{k}}) - \cos(\theta_{\mathbf{k}+\mathbf{q}})}{2}, \end{aligned} \quad (17)$$

We notice that around the Γ point Fermi surface, $\theta_{\mathbf{k}}$ changes from 0 to 4π ; around the M point, $\theta_{\mathbf{k}}$ changes from 0 to π and then back to 0. In either case, we have $\int_{k_f} \cos(\theta_k) d^2k \sim 0$, and therefore the inter-orbit scattering is always much smaller than the intra-orbit scattering, which is also seen in Fig. 3.

III. FIVE-ORBITAL MODEL AND NUMERICAL RESULTS

A better fit to the LDA band structure in iron-based superconductors is given by a five orbital proposed in⁴³. To investigate the model-dependence of the scattering patterns, we now perform all the above calculations employing this five-orbital model augmented by an intra-orbital $s_x^2y^2$ pairing symmetry.

In Fig. 11, we show the bulk DOS for the clean system. The coherence peaks appear at ± 0.082 and the system is fully gapped within $\sim (-0.05, 0.05)$. In Fig. 12, we plot the spectral function $\mathcal{A}(\mathbf{k}, \omega)$ in the unfolded Brillouin zone, where the energy contours and their weight can be

the form

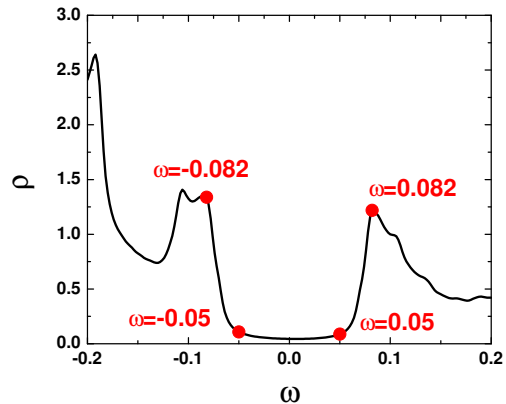


FIG. 11: Bulk density of states ρ for five-orbital model with $s_x^2y^2$ pairing as a function of ω , $\Delta_0 = 0.1$ and no impurities. The energy broadening width $\delta = 0.002$.

clearly seen. In Fig. 13 and Fig. 14, we plot the interference pattern $\delta\rho(\mathbf{q})$ for non-magnetic and magnetic impurities, respectively. Their profiles in the direction $M \rightarrow \Gamma \rightarrow \Gamma'$ are plotted in Fig. 15. Finally, for comparison, we also plot the results for order parameter without sign change in Fig. 16.

It is clear that the QPI in the five orbital model is quite different from that in the two orbital model. This major difference comes from the distribution of density of states at the Fermi surfaces. For example, compared with the QPI in the two-orbital model, scattering around Γ now has its origin in the intra-pocket scattering within the hole pockets - in the two orbital model it originates from intra-electron pocket scattering. The density of states is higher in the electron than in the hole pockets in the two band model. The opposite is true in the five orbital model. Another clear difference is that due to the existence of additional orbitals, there exist square shaped profiles in Fig. 13 (b) and (c) which correspond to the scattering process labeled by arrow 1 in Fig. 12 (b); and the circle shaped profile in Fig. 13 (d) corresponds to arrow 2. These features are absent in the two orbital model.

However, there are also common features in both models. The broad and large peaks at $\mathbf{q} = (0, 0)$ for mag-

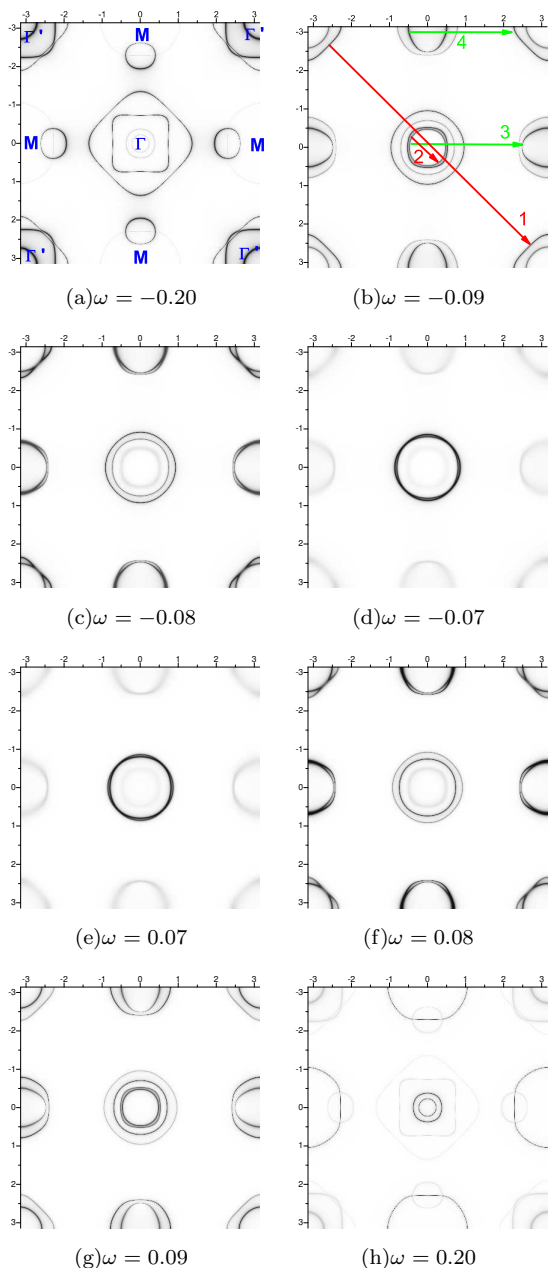


FIG. 12: The spectral function $\mathcal{A}(\mathbf{k}, \omega)$ in the unfolded Brillouin zone, for five-orbital model with $\Delta_0 = 0.1$. Darker regions correspond to larger values of \mathcal{A} hence larger DOS in \mathbf{k} space.

netic impurity appear in both models. More importantly, the $(\pm\pi, 0)/(0, \pm\pi)$ sensitiveness on magnetic or non-magnetic impurity, and sign change remains the same. For example, when Δ changes sign, the peak around $\mathbf{q} = (\pm\pi, 0)/(0, \pm\pi)$ for non-magnetic impurity (Fig. 15 (a)) disappears in the case of a magnetic impurity (Fig. 15 (b)). On the contrary, when Δ does NOT change sign (Fig. 16), the peak at $(\pm\pi, 0)/(0, \pm\pi)$ is related to magnetic impurity. The sensitiveness of the interference pattern around $(\pm\pi, 0)/(0, \pm\pi)$ corresponds to the inter-pocket scattering labeled by arrows 3 and 4 in Fig. 12

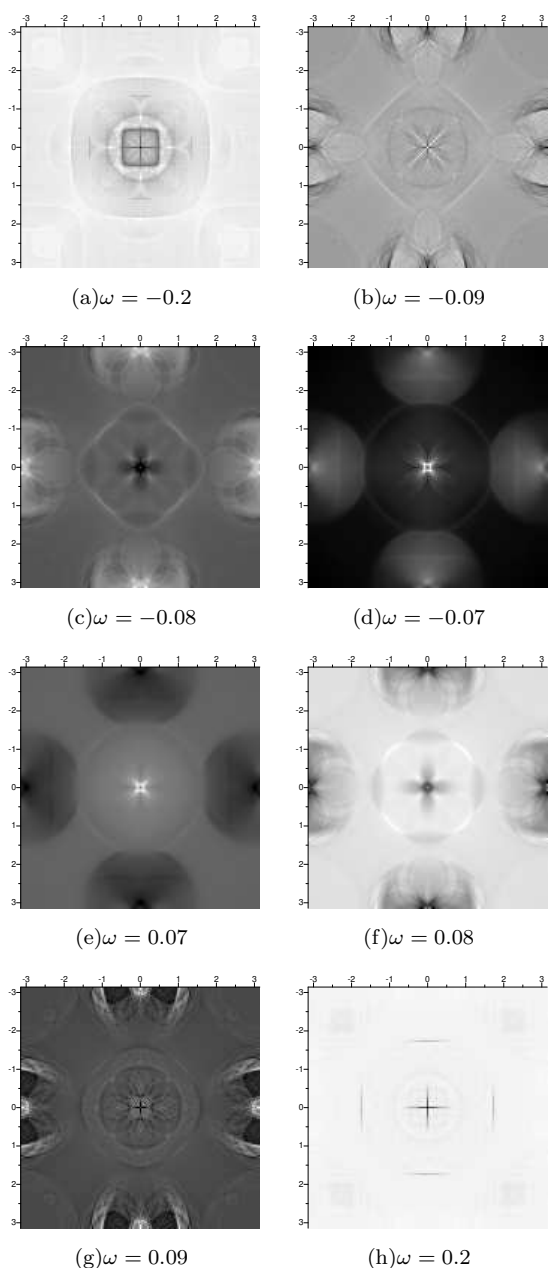


FIG. 13: $\delta\rho(\mathbf{q})$ for five-orbital model, non-magnetic impurity with intra-orbital scattering, $V_0 = 0.4$. A 160×160 lattice in \mathbf{k} -space is used in numerical integration of equation (5) and the energy broadening width $\delta = 0.001$.

(b) and has been explained explicitly in the two-orbital model. Eqs. (14) and (15) and the arguments following them do not depend on the number of bands and therefore these features are rather universal. Moreover, the $(\pm\pi, 0)/(0, \pm\pi)$ sensitiveness on the order parameter sign change (Fig. 16) is quite similar with the two-orbital model.

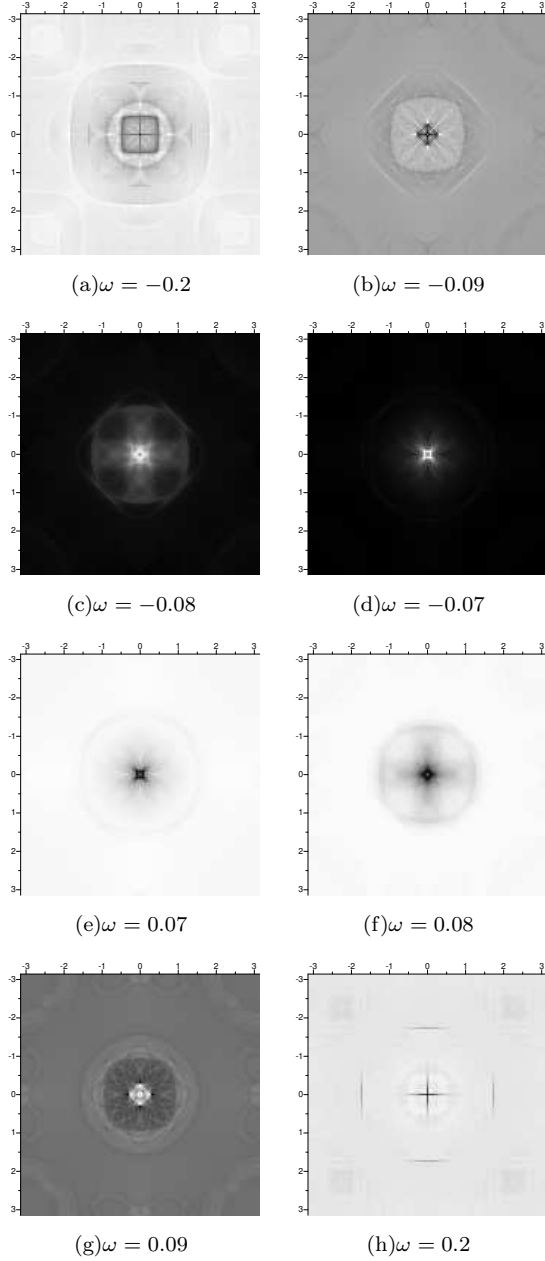


FIG. 14: Same as Fig. 13 but for magnetic impurity, $V_0 = 0.4$.

IV. CONCLUSION

In summary, we have investigated in detail the structures of the QPI in iron-based superconductors within the current available two orbital and five orbital models. The results obtained here suggest that the QPI can be used to determine the band structure and orbital degrees of freedom in these materials and can also provide evidence of the SC pairing symmetries. In this calculation, we have ignored possible three dimensional effects, more relevant for the 122 materials^{44,45}. The physics associ-

ated with the third dimension and possible competing orders or coexistence states will be addressed in the fu-

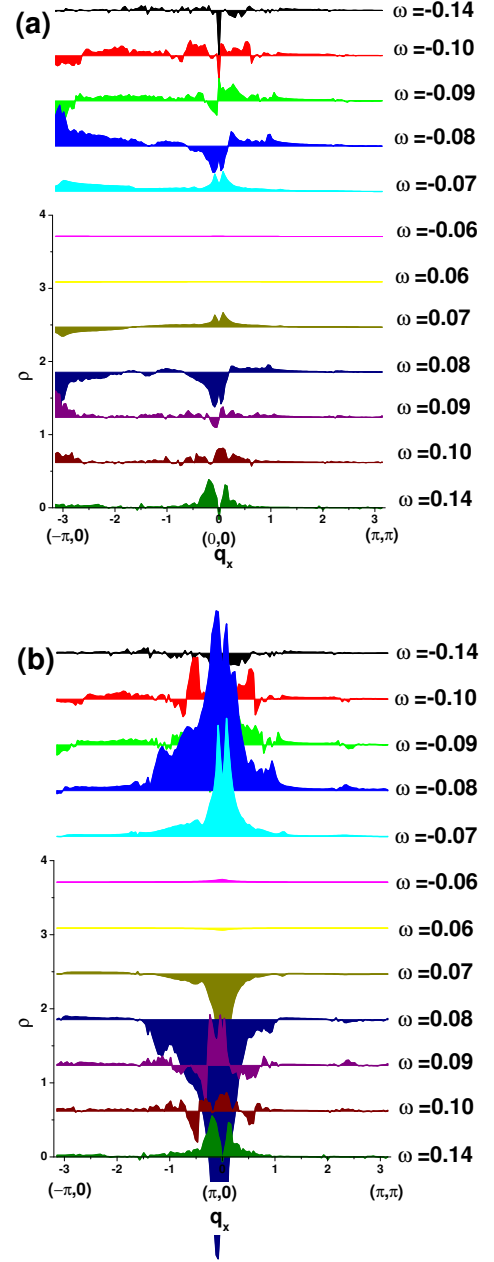


FIG. 15: (color online) Profiles of $\delta\rho(\mathbf{q}, \omega)$ along $M \rightarrow \Gamma \rightarrow \Gamma'$ for (a) non-magnetic impurity and (b) magnetic impurity in five-orbital model.

ture.

Acknowledge: JPH and BAB thanks Dunghai Lee for useful discussions. JPH, YYZ, WFT, XTZ, KJS and CF were supported by the NSF under grant No. PHY-0603759.

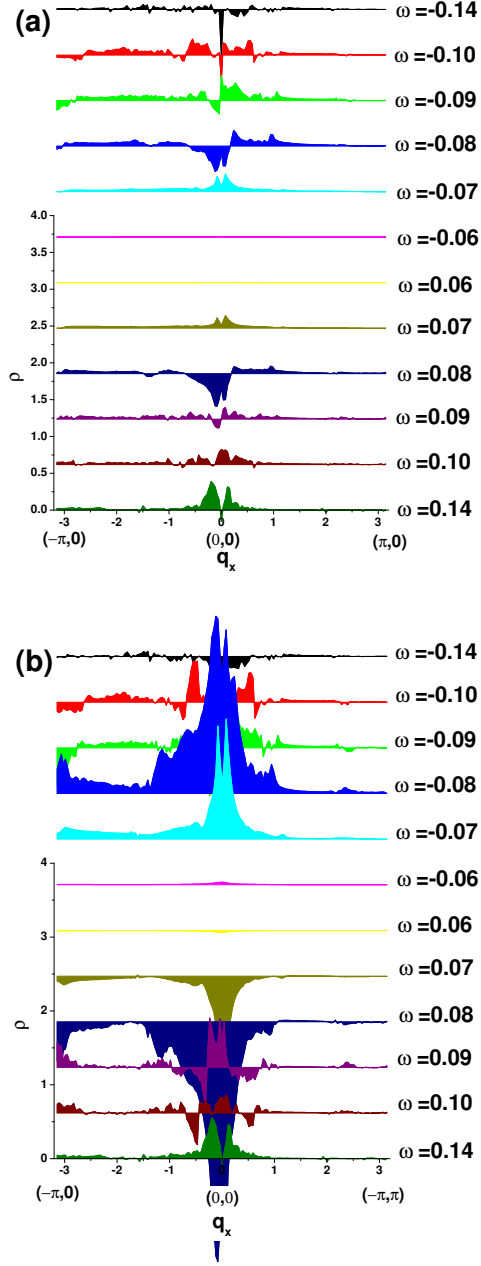


FIG. 16: (color online) Same as Fig. 15 but for the case without sign change of Δ .

- ¹ Y. Kamihara, T. Watanabe, M. Hirano, and H. Hosono, *J. Am. Chem. Soc.* **130**, 3296 (2008).
- ² H. Takahashi, K. Igawa, K. Arii, Y. Kamihara, M. Hirano, and H. Hosono, *Nature* **453**, 376 (2008).
- ³ X. H. Chen, T. Wu, G. Wu, R. H. Liu, H. Chen, and D. F. Fang, *Nature* **453**, 761 (2008).
- ⁴ H.-H. Wen, G. Mu, L. Fang, H. Yang, and X. Zhu, *Europhys. Lett.* **82**, 17009 (2008).
- ⁵ G. F. Chen, Z. Li, D. Wu, G. Li, W. Z. Hu, J. Dong, P.

- Zheng, J. L. Luo, and N. L. Wang, *Physical Review Letters* **100**, 247002 (2008).
- ⁶ K. Seo, B. A. Bernevig, and J. Hu, *Phys. Rev. Lett* **101**, 206404 (2008).
- ⁷ I. I. Mazin, D. J. Singh, M. D. Johannes, and M. H. Du, *Phys. Rev. Lett* **101**, 057003 (2008).
- ⁸ F. Wang, H. Zhai, and D.-H. Lee, *EPL* **85**, 37005 (2009).
- ⁹ C. Fang, H. Yao, W.-F. Tsai, J. Hu, and S. A. Kivelson, *Phys. Rev. B* **77**, 224509 (2008).

- ¹⁰ T. Yildirim, Phys. Rev. Lett **101**, 057010 (2008).
- ¹¹ Q. Si and E. Abrahams, Phys. Rev. Lett **076401**, arXiv:0804.2480 (2008).
- ¹² H. Ding, P. Richard, K. Nakayama, T. Sugawara, T. Arakane, Y. Sekiba, A. Takayama, S. Souma, T. Sato, T. Takahashi, Z. Wang, X. Dai, Z. Fang, G. F. Chen, J. L. Luo, and N. L. Wang, Europhys. Lett. **83**, 47001 (2008).
- ¹³ K. Nakayama, T. Sato, P. Richard, Y.-M. Xu, Y. Sekiba, S. Souma, G. F. Chen, J. L. Luo, N. L. Wang, H. Ding, and T. Takahashi, arXiv:0812.0663 (2008).
- ¹⁴ L. Wray, D. Qian, D. Hsieh, Y. Xia, L. Li, J. Checkelsky, A. Pasupathy, K. Gomes, A. Fedorov, G. Chen, J. Luo, A. Yazdani, N. Ong, N. Wang, and M. Hasan, arXiv:0808.2185 (2008).
- ¹⁵ M. M. Parish, J. Hu, and B. A. Bernevig, Phys. Rev. B **78**, 144514 (2008).
- ¹⁶ D. Parker, O. V. Dolgov, M. M. Korshunov, A. A. Golubov, and I. I. Mazin, arXiv:0807.3729 (2008).
- ¹⁷ M. S. Laad and L. Craco, arXiv:0902.3400 (2009).
- ¹⁸ T. A. Maier and D. J. Scalapino, Phys. Rev. B **78**, 020514 (2008).
- ¹⁹ W.-F. Tsai, D.-X. Yao, B. Bernevig, and J. Hu, arXiv:0812.0661 (2008).
- ²⁰ P. Ghaemi, F. Wang, and A. Vishwanath, arXiv:0812.0015 (2008).
- ²¹ D. Parker and I. Mazin, arXiv:0812.4416 (2008).
- ²² J. Wu and P. Phillips, arXiv:0901.0038 (2009).
- ²³ J. E. Hoffman *et al.*, Science **295**, 466 (2002).
- ²⁴ Q.-H. Wang and D.-H. Lee, Phys. Rev. B **67**, 020511(R) (2003).
- ²⁵ K. McElroy *et al.*, Nature (London) **422**, 592 (2003).
- ²⁶ K. McElroy *et al.*, Physica C **388**, 225 (2003).
- ²⁷ H. D. Chen, O. Vafek, A. Yazdani, and S. C. Zhang, Phys. Rev. Lett. **93**, 187002 (2004).
- ²⁸ K. Seo, H.-D. Chen, and J. Hu, Phys. Rev. B **76**, 020511(R) (2007).
- ²⁹ K. Seo, H.-D. Chen, and J. Hu, Phys. Rev. B **78**, 094510 (2008).
- ³⁰ H. D. Chen, J. P. Hu, S. Capponi, E. Arrigoni, and S. C. Zhang, Phys. Rev. Lett. **89**, 137004 (2002).
- ³¹ H.-D. Chen, S. Capponi, F. Alet, and S.-C. Zhang, Phys. Rev. B **70**, 024516 (2004).
- ³² C. Bena, S. Chakravarty, J. Hu, and C. Nayak, Phys. Rev. B **69**, 134517 (2004).
- ³³ A. Ghosal, A. Kopp, and S. Chakravarty, Phys. Rev. B **72**, 220502(R) (2005).
- ³⁴ Z. Tesanovic, Phys. Rev. Lett. **93**, 217004 (2004).
- ³⁵ A. Melikyan and Z. Tesanovic, Phys. Rev. B **71**, 214511 (2005).
- ³⁶ S. Sachdev and E. Demler, Phys. Rev. B **69**, 144504 (2004).
- ³⁷ S. A. Kivelson *et al.*, Rev. Mod. Phys. **75**, 1201 (2003).
- ³⁸ J. A. Robertson *et al.*, cond-mat/0602675.
- ³⁹ D. Podolsky, E. Demler, K. Damle, and B. I. Halperin, Phys. Rev. B **67**, 094514 (2003).
- ⁴⁰ T. Pereg-Barnea and M. Franz, Phys. Rev. B **68**, 180506 (2003).
- ⁴¹ L. Capriotti, D. Scalapino, and R. Sedgewick, Phys. Rev. B **68**, 014508 (2003).
- ⁴² S. Raghu, X.-L. Qi, C.-X. Liu, D. Scalapino, and S.-C. Zhang, Phys. Rev. B **77**, 22503 (2008).
- ⁴³ K. Kuroki, S. Onari, R. Arita, H. Usui, Y. Tanaka, H. Kontani, and H. Aoki, Phys. Rev. Lett. **101**, 087004 (2008).
- ⁴⁴ J. Zhao, D.-X. Yao, S. Li, T. Hong, Y. Chen, S. Chang, W. Ratcli, J. W. Lynn, H. A. Mook, G. F. Chen, J. L. Luo, N. L. Wang, E. W. Carlson, J. Hu, and P. Dai, Phys. Rev. Lett **101**, 167203 (2008).
- ⁴⁵ H. Q. Yuan, J. Singleton, F. F. Balakirev, S. A. Baily, G. F. Chen, J. L. Luo, and N. L. Wang, Nature **457**, 565 (2009).